

## Enhanced degradation of micropollutants by UV/freshly formed colloidal MnO<sub>2</sub>: Reactive species, kinetics and pathways

Wenrui Wei, Anna Wang, Kaiheng Guo, Shaoxiong He, Ailin Li, Xinwen Kang, Jingyun Fang <sup>\*</sup>

Guangdong Provincial Key Laboratory of Environmental Pollution Control and Remediation Technology, School of Environmental Science and Engineering, Sun Yat-Sen University, Guangzhou 510275, China



### ARTICLE INFO

#### Keywords:

Freshly formed colloidal manganese dioxide  
Photocatalyst  
Micropollutants  
Reactive species  
Water treatment

### ABSTRACT

This study reports that freshly formed manganese dioxide (MnO<sub>2</sub>) is an effective photocatalyst for the abatement of micropollutants, such as nalidixic acid (NDA) and gemfibrozil (GFRZ). The freshly formed MnO<sub>2</sub> was flower-like  $\beta$ -MnO<sub>2</sub> and showed better efficiency in micropollutant abatement owing to its better adsorption capability than commercial MnO<sub>2</sub>. Electron paramagnetic resonance (EPR) spectra confirmed that reactive oxygen species (ROS), including hydroxyl radicals (HO<sup>•</sup>), superoxide radicals (O<sub>2</sub><sup>•</sup>) and singlet oxygen (<sup>1</sup>O<sub>2</sub>), were formed in the UV/MnO<sub>2</sub> system. Valence band X-ray photoelectron spectroscopy (VB-XPS) spectra and UV-vis adsorption curves verified the generation of ROS via the reaction between e<sup>-</sup> and oxygen as the sole pathway. Holes (h<sup>+</sup>) dominated the degradation of NDA, while both ROS and h<sup>+</sup> were important for GFRZ abatement. Side chain cleavage, kentonization and hydroxylation took place in NDA and GFRZ degradation, while demethylation and decarboxylation also occurred during NDA degradation.

### 1. Introduction

Manganese is one of the most abundant metallic elements on Earth [1], and manganese compounds, such as permanganate and manganese dioxide (MnO<sub>2</sub>), are important to the transformation of organic pollutants in engineered and natural aqueous systems [2,3]. MnO<sub>2</sub> widely occurs in natural water and sediments [4] and participates in transforming some micropollutants via adsorption and/or oxidation [4–6]. Meanwhile, MnO<sub>2</sub> has been widely used as or to synthesize thermo-, electro- and photocatalysts [7]. As a reduction product of permanganate, colloidal MnO<sub>2</sub> can be formed in situ during permanganate pre-oxidation in water treatment [6]. Additionally, recent studies have reported that colloidal MnO<sub>2</sub> with an average size of 50 nm could form in manganese ion-based and permanganate-based water treatment processes [8,9]. Recent studies investigated the adsorption efficiency of micropollutants by various types of photocatalysts such as TiO<sub>2</sub> and commercial MnO<sub>2</sub>. The removal rates of micropollutants such as phenols, benzoates and gemfibrozil via MnO<sub>2</sub> adsorption were less than 10% within 2 h [10–12]. Unlike typical particle photocatalysts, recent studies elucidated better adsorption capacity of freshly formed colloidal MnO<sub>2</sub> owing to the rich -OH groups at the surface [13,14], which may enhance the photocatalysis capacity. Thus, the fate of freshly formed colloidal

MnO<sub>2</sub> for micropollutant abatement requires investigation.

MnO<sub>2</sub> is known to act as a photocatalyst upon UV irradiation [7, 15–17]. Recent studies on MnO<sub>2</sub> photocatalytic systems have mainly focused on synthesized MnO<sub>2</sub>-based materials. UV irradiation of commercial MnO<sub>2</sub> has been reported for the inactivation of pathogens [17], decolorization [18,19], and wastewater treatment [20]. However, the photocatalytic fate of freshly formed colloidal MnO<sub>2</sub> has not been investigated, which is different from that of commercial MnO<sub>2</sub>. Thus, the UV photocatalysis of freshly formed colloidal MnO<sub>2</sub> should be clarified.

According to the photocatalytic mechanisms, photogenerated holes (h<sup>+</sup>) and electrons (e<sup>-</sup>) are primarily generated when applying UV irradiation to commercial MnO<sub>2</sub> [21]. Then, secondary reactive oxygen species (ROS), including hydroxyl radicals (HO<sup>•</sup>) and superoxide radicals (O<sub>2</sub><sup>•</sup>), can be generated from h<sup>+</sup> or e<sup>-</sup> [7,22]. However, there are several unknowns in the UV/MnO<sub>2</sub> system for pollutant removal. First, the generation pathways of ROS are quite inconsistent. Some studies suggest that HO<sup>•</sup> is formed via the reaction between h<sup>+</sup> and H<sub>2</sub>O/OH<sup>-</sup> [18,21,23–25], while others claim that ROS are totally formed through the reactions between e<sup>-</sup> and O<sub>2</sub> [15,19,20,26]. In addition, the specific contribution of different reactive species to the degradation kinetics and transformation pathways of micropollutants by the UV/MnO<sub>2</sub> system is unclear.

\* Corresponding author.

E-mail address: [fangjy3@mail.sysu.edu.cn](mailto:fangjy3@mail.sysu.edu.cn) (J. Fang).

Thus, the objectives of this study were to investigate the chemistry of reactive species in the UV/colloidal  $\text{MnO}_2$  system for the abatement of micropollutants. The contribution of different reactive species and the degradation pathways were clarified. Two common pharmaceuticals and personal care products (PPCPs), nalidixic acid (NDA) and gemfibrozil (GFRZ), were selected as the target micropollutants, as they are widely detected in aqueous systems [27,28]. NDA is a typical quinolone antibacterial widely used for urinary tract infections [29], and GFRZ, as a lipid regulator, can efficiently treat hypercholesterolemia [30]. Although NDA and GFRZ were detected at trace levels ranging from 50 to 2500 ng  $\text{L}^{-1}$  in natural water, their persistence and bioaccumulation effect can pose potential risks to aqueous environment and human health [30,31]. Moreover, the effects of  $\text{MnO}_2$  dosage, pH and common water matrices, including natural organic matter (NOM), bicarbonate ( $\text{HCO}_3^-$ ), chloride ( $\text{Cl}^-$ ) and sulphate ions ( $\text{SO}_4^{2-}$ ), were investigated.

## 2. Materials and methods

### 2.1. Chemicals

All solutions were prepared with reagent-grade chemicals and Milli-Q water (18.2  $\text{M}\Omega \text{ cm}$ ). GFRZ, NDA, 2,2-azino-bis(3-ethylbenzothiazoline)-6-sulfonic acid diammonium (ABTS) and nitrobenzene (NB) were obtained from Sigma-Aldrich (St. Louis, MO, USA). The specific properties of NDA and GFRZ are shown in Table S1. Methanol ( $\text{CH}_3\text{OH}$ ), acetonitrile ( $\text{CH}_3\text{CN}$ ) and *o*-phosphoric acid for high-performance liquid chromatography (HPLC) and *tert*-butanol (TBA) were purchased from Fisher Scientific (USA). Commercial  $\text{MnO}_2$  particles were purchased from J&K Scientific Ltd. (Beijing, China), and detailed information is shown in Table 1.  $\text{KMnO}_4$ ,  $\text{MnCl}_2$ ,  $\text{Na}_2\text{SO}_4$ ,  $\text{NaCl}$ ,  $\text{NaHCO}_3$ , boric acid, sodium borate and sodium oxalate were purchased from Sinopharm Chemical Reagent Co., Ltd. (Shanghai, China). Argon (>99.9%) was purchased from Messer (Germany). Suwannee River natural organic matter (NOM) (cat. no. 2R101N) obtained from the International Humic Substances Society was dissolved in pure water and filtered through a 0.45- $\mu\text{m}$  membrane to prepare a stock NOM solution.

### 2.2. Synthesis and characterization of colloidal $\text{MnO}_2$

Freshly formed colloidal  $\text{MnO}_2$  was synthesized using the reaction of  $\text{MnCl}_2$  and  $\text{KMnO}_4$ . Briefly,  $\text{MnCl}_2$  (60  $\mu\text{M}$ ) and  $\text{KMnO}_4$  (40  $\mu\text{M}$ ) were mixed to generate  $\text{MnO}_2$  (100  $\mu\text{M}$ ), which was brownish yellow. The particle size distribution of colloidal  $\text{MnO}_2$  was determined by a laser particle size analyser (Malvern, Mastersizer 3000, UK). The average manganese valence of colloidal  $\text{MnO}_2$  was determined by ABTS method [32] with details shown in Text S1. The colloidal  $\text{MnO}_2$  was freeze-dried to obtain powder  $\text{MnO}_2$  for characterization. X-ray powder diffraction (XRD, RIGAKU, UltimaIV, Japan) was employed to obtain the crystal phase information of  $\text{MnO}_2$ . Images of the  $\text{MnO}_2$  formed in this study were obtained via scanning electron microscopy (SEM, Zeiss Sigma 500, Germany). The specific surface areas were measured using nitrogen adsorption-desorption isotherms at 77 K, according to Brunauer-Emmett-Teller analysis (BET, Beijing JWGB Ltd., JW-BK200C, China). The relative position of the valence band (VB) of  $\text{MnO}_2$  was obtained by X-ray photoelectron spectroscopy (XPS, Thermo Fisher ESCALAB 250, USA). UV-vis adsorption curves of  $\text{MnO}_2$  were obtained

Table 1

The parameters of freshly formed  $\text{MnO}_2$  and the used commercial  $\text{MnO}_2$ .

| Materials                     | XRD pattern           | JCPDS No. | Average size (nm) | Specific surface areas ( $\text{m}^2 \text{ g}^{-1}$ ) |
|-------------------------------|-----------------------|-----------|-------------------|--|
| Freshly formed $\text{MnO}_2$ | $\beta\text{-MnO}_2$  | 81-2261   | 50.3              | 47.89  |
| Commercial $\text{MnO}_2$     | $\alpha\text{-MnO}_2$ | 44-0141   | 80.0              | 18.83  |

using a UV-vis spectrophotometer (PerkinElmer, Lambda 950, USA) with integral-sphere attachment ranging from 400 to 800 nm, which helped obtain the band gap energies ( $E_g$ ) and relative position of the conduction band (CB).

### 2.3. Experimental procedures

The photochemical experiments were performed in a 700-mL magnetically stirred cylindrical borosilicate glass reactor with a quartz tube in the centre in which a low-pressure mercury lamp (Heraeus GPH 212T5L/4, 10 W) was placed. The reactor temperature was controlled at  $25 \pm 0.2$  °C by a water circulating system. The average UV fluence rate was determined to be 5.24 mW  $\text{cm}^{-2}$  by iodide/iodate chemical actinometry [33]. The effective path length of the photochemical reactor was determined to be 3.47 cm by measuring the photolysis kinetics of dilute  $\text{H}_2\text{O}_2$  [8].

$\text{MnO}_2$  (100  $\mu\text{M}$ ) was first buffered at pH 6.0 – 8.0 (borate buffer, 5 mM), and the target compounds (NDA and GFRZ for each concentration of 5  $\mu\text{M}$ ) and 1  $\mu\text{M}$  NB were added into the testing solution and mixed for 5 min to reach adsorption equilibrium. Then, a UV lamp was placed into the reactor to start the reaction. Samples were collected at pre-determined time intervals, and colloidal  $\text{MnO}_2$  was dissolved by excessive ascorbic acid and then filtered through a 0.22- $\mu\text{m}$  membrane. To investigate the adsorption capacity of colloidal  $\text{MnO}_2$ , 4-mL samples were collected and filtered by a centrifugal filter unit (10 kDa, Merck Millipore Ltd.). NB was employed to probe the  $\text{HO}^\bullet$  concentration and further quantify the contribution of  $\text{HO}^\bullet$  to micropollutant abatement [34], and the detailed information is shown in Text S2. Control tests, which involved exposure to either UV photolysis or  $\text{MnO}_2$  alone, were carried out in a similar manner in the absence of  $\text{MnO}_2$  and UV. TBA, sodium oxalate, and argon were added to the testing solution to quench  $\text{HO}^\bullet$ ,  $\text{h}^+$  and ROS, respectively, and to calculate the contribution of each species. An orthogonal matrix experimental design was used to investigate the effect of parameters, including the  $\text{MnO}_2$  dosage, pH, NOM,  $\text{HCO}_3^-$ ,  $\text{Cl}^-$ , and  $\text{SO}_4^{2-}$ , in the UV/ $\text{MnO}_2$  system. Additionally, to study the degradation pathways of NDA and GFRZ by the UV/colloidal  $\text{MnO}_2$  system, the samples for identification of the generated products of NDA and GFRZ were pre-treated by solid-phase extraction (SPE) before analysis.

### 2.4. Analytical methods

The concentrations of NDA and GFRZ were determined by an HPLC system (Agilent 1260, USA) equipped with an Agilent ZORBAX SB-C18 HD column (4.6 mm  $\times$  150 mm, 5- $\mu\text{m}$  particle size) and a DAD detector to separate the target pollutants (details shown in Table S2). The concentration of  $\text{MnO}_2$  was detected via a UV-visible spectrophotometer (Shimadzu, UV-2600) at 200–800 nm.

Electron paramagnetic resonance (EPR) spectroscopy (Bruker EMX-nano spectrometer, Germany) was applied to investigate reactive species generation. 5,5-Dimethyl-1-pyrroline N-oxide (DMPO) was used as the spin trapping reagent for  $\text{HO}^\bullet$  and  $\text{O}_2^\bullet^-$ , while 2,2,6,6-tetramethylpiperidine (TEMP) was used as the spin trapping reagent for  $^1\text{O}_2$ .

The transformation products of NDA and GFRZ were concentrated by solid-phase extraction (SPE) using hydrophile lipophilic balance (HLB) cartridges (200 mg, 6 mL, CNW) and then identified using an ultra-high-performance liquid chromatography quadrupole time-of-flight mass spectrometer (UPLC-Q-TOF-MS) (Waters Synapt G2-Si, USA) equipped with an electrospray interface (ESI). The products of NDA were identified in both positive ( $\text{ES}^+$ ) and negative ( $\text{ES}^-$ ) modes. The products of GFRZ were identified in  $\text{ES}^-$  mode. The details of the chromatographic and mass conditions for UPLC-QTOF-MS analysis are described in Text S3.

### 3. Results and discussion

#### 3.1. Characterization of freshly formed colloidal $MnO_2$

Fig. 1a shows that the particle size distribution of freshly formed  $MnO_2$  was concentrated at 0–400 nm with an average size of 50.3 nm, indicating the formation of colloidal  $MnO_2$ . The XRD spectrum shows diffraction peaks at  $28.4^\circ$ ,  $37.9^\circ$ ,  $40.5^\circ$ ,  $59.2^\circ$  and  $64.9^\circ$ , corresponding to the (110), (101), (111), (211) and (002) crystalline planes of  $\beta$ - $MnO_2$ , which also match that of  $\beta$ - $MnO_2$  (JCPDS card no. 81-2261) [35], as shown in Fig. 1b. Furthermore, the morphologies and microstructures characterized by scanning electron microscopy (SEM) show a flower-like surface structure (Fig. 1c). The XRD pattern, average size and specific surface area of each kind of  $MnO_2$  used in the study are shown in Table 1

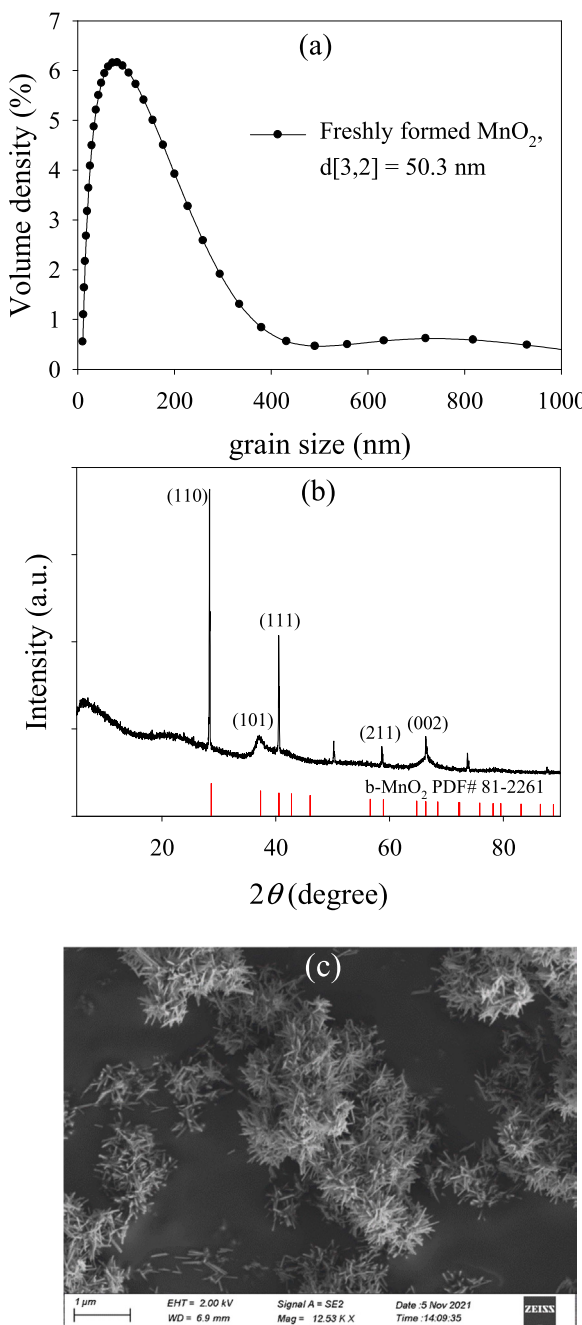


Fig. 1. Particle size distribution (a), XRD spectrum (b), and SEM image (c) of freshly formed colloidal  $MnO_2$ .

and Fig. S3. The XRD spectrum of commercial  $MnO_2$  particles matched that of  $\alpha$ - $MnO_2$  (JCPDS card no. 44-0141) with an average size of 80.0 nm. The specific surface areas of freshly formed colloidal  $MnO_2$  and commercial  $MnO_2$  are 47.89 and  $18.83 \text{ m}^2 \text{ g}^{-1}$ , respectively.

#### 3.2. Degradation of NDA and GFRZ by the UV/ $MnO_2$ system

Fig. 2 shows the degradation of NDA and GFRZ by the UV/ $MnO_2$  system at pH 7 in pure water. Both NDA and GFRZ were resistant to freshly formed colloidal  $MnO_2$  alone, indicating the negligible oxidation by  $MnO_2$ . In comparison, NDA and GFRZ were efficiently degraded by the UV/ $MnO_2$  system, with pseudo-first-order rate constants ( $k$ 's) of 0.299 and 0.116  $\text{min}^{-1}$ , respectively, which were 6.1 and 2.4 times higher than those by UV photolysis. The remarkable degradation of NDA and GFRZ in UV/ $MnO_2$  indicates the contribution of the formed reactive species. In addition, the time-dependent UV-vis spectra of  $MnO_2$  in the UV/ $MnO_2$  system showed no obvious change within 20 min (Fig. S1), which differed from the rapid consumption of  $MnO_2$  as an oxidant for the degradation of anilines and phenols [36]. Meanwhile, the average manganese valence of freshly formed colloidal  $MnO_2$  retained at 4.04 ( $\pm 0.04$ ) (Fig. S2), which further confirmed its stability. Moreover, photocatalytic effects of the freshly formed colloidal  $MnO_2$  and other 5 kinds of  $MnO_2$  and 2 kinds of  $TiO_2$  were compared, and the details are shown in Table S3. Obviously, the removal efficiencies of the target pollutants by using freshly formed colloidal  $MnO_2$  were much higher than the other photocatalysts [23,37–42], evidencing the effective

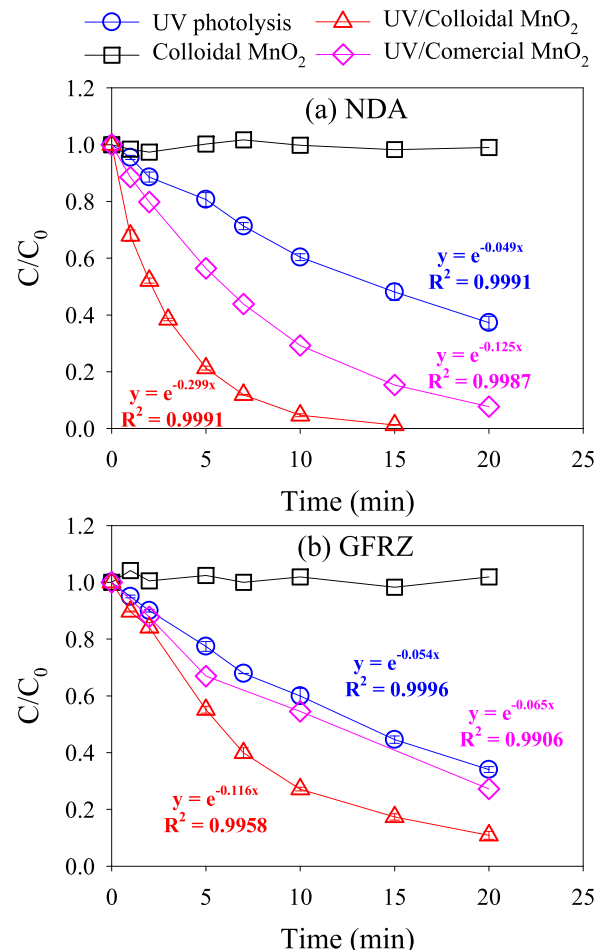


Fig. 2. Degradation of (a) NDA and (b) GFRZ in  $MnO_2$  alone, UV irradiation, and the UV/freshly formed colloidal  $MnO_2$  and UV/commercial  $MnO_2$  systems at pH 7.0 in pure water. Conditions:  $[MnO_2]_0 = 100 \mu\text{M}$ ,  $[GFRZ]_0 = [NDA]_0 = 5 \mu\text{M}$ .

photocatalytic capacity of the freshly formed  $\text{MnO}_2$  used here. Also, main products of NDA and GFRZ formed in UV/freshly formed colloidal  $\text{MnO}_2$  system and UV photolysis were compared in Tables S4 – S7. Obviously, for NDA, compared with UV photolysis, 10 different main products, especially ring-cleavage products of  $m/z$  225 ( $\text{C}_{10}\text{H}_{13}\text{N}_2\text{O}_4$ ),  $m/z$  253 ( $\text{C}_{12}\text{H}_{17}\text{N}_2\text{O}_4$ ) and  $m/z$  239 ( $\text{C}_{10}\text{H}_{11}\text{N}_2\text{O}_5$ ) were found in UV/freshly formed colloidal  $\text{MnO}_2$  system. Meanwhile, for GFRZ, different isomers of  $m/z$  263 ( $\text{C}_{15}\text{H}_{20}\text{O}_4$ ),  $m/z$  135 ( $\text{C}_8\text{H}_8\text{O}_2$ ) and  $m/z$  265 ( $\text{C}_{15}\text{H}_{22}\text{O}_4$ ) were found in UV/freshly formed colloidal  $\text{MnO}_2$  system. These results prove that freshly formed colloidal  $\text{MnO}_2$  acted as an effective photocatalyst.

The photocatalytic effect of freshly formed colloidal  $\text{MnO}_2$  in this study and commercial  $\text{MnO}_2$  particles was also compared. As shown in Fig. 2, the  $k$ 's of NDA and GFRZ by UV/freshly formed  $\text{MnO}_2$  were 139.2% and 78.5% higher than those by the UV/commercial  $\text{MnO}_2$  system, respectively. The higher photocatalytic capacity of the freshly formed colloidal  $\text{MnO}_2$  can be explained as follows. It is obvious that freshly formed colloidal  $\text{MnO}_2$  exhibited a much larger specific surface area ( $47.89 \text{ m}^2 \text{ g}^{-1}$ ), which was 2.5-fold larger than commercial  $\text{MnO}_2$  ( $18.83 \text{ m}^2 \text{ g}^{-1}$ ) (Table 1). A higher specific surface area indicated a better adsorption capacity [43]. Meanwhile, the surface of colloidal  $\text{MnO}_2$  was rich in -OH groups, thus it could adsorb micropollutants containing -COOH [4,13,14]. As shown in Fig. S4, the adsorption rates of NDA and GFRZ by equimolar commercial  $\text{MnO}_2$  were less than 5%, while those by freshly formed colloidal  $\text{MnO}_2$  were much higher at 71.5% and 58.3% within 5 min. The higher surface adsorption capacity of the photocatalyst allows reactive species, especially  $\text{h}^+$ , to attack pollutants effectively [44].

Moreover, to investigate the photocatalytic stability of freshly

formed colloidal  $\text{MnO}_2$ , five cycle experiments were consecutively conducted, as shown in Fig. S5. Compared with the first cycle, the  $k$ 's of NDA and GFRZ after 5 cycles dropped by 25.8% and 26.7%, respectively, presumably due to the loss of surface adsorption capacity. Nevertheless, the removal efficiencies of NDA and GFRZ still reached 99% and 82%, respectively, at 20 min after 5 cycles.

### 3.3. Identification of reactive species in the UV/ $\text{MnO}_2$ system

To further clarify the mechanisms of enhanced degradation by UV/ $\text{MnO}_2$ , the specific roles of reactive species responsible for the degradation of NDA and GFRZ were quantified. First, EPR spectroscopy was employed to determine the formation of reactive species in the UV/freshly formed colloidal  $\text{MnO}_2$  and UV/commercial  $\text{MnO}_2$  systems. DMPO was used as a spin trapping reagent of  $\text{HO}^\bullet$  and  $\text{O}_2^\bullet-$  [8,45]. As shown in Fig. 3, a typical 1:2:2:1 quartet signal of the DMPO-OH spin adduct and six representative signals of the DMPO- $\text{O}_2^\bullet-$  adduct were detected in both systems. Meanwhile, TEMP was used as a trapping agent of singlet oxygen ( $^1\text{O}_2$ ), as  $^1\text{O}_2$  can oxidize TEMP to form a typical triplet signal of 2,2,6,6-tetramethyl-1-piperidinyloxy (TEMPO) [46]. In this study, the TEMPO signal was detected in both UV/freshly formed  $\text{MnO}_2$  and UV/commercial  $\text{MnO}_2$  systems, whose intensity was significantly higher than that in UV or  $\text{MnO}_2$  alone, indicating the formation of  $^1\text{O}_2$ . However, the intensities of the signals in UV/freshly formed colloidal  $\text{MnO}_2$  are 1.7-folds (DMPO-OH), 1.6-folds (DMPO- $\text{O}_2^\bullet-$ ) and 1.6-folds (TEMPO) higher than that in UV/commercial  $\text{MnO}_2$  process, suggesting that ROS was formed in UV/ freshly formed colloidal  $\text{MnO}_2$  system more efficiently.

Mechanistic insights into the formation of reactive species were

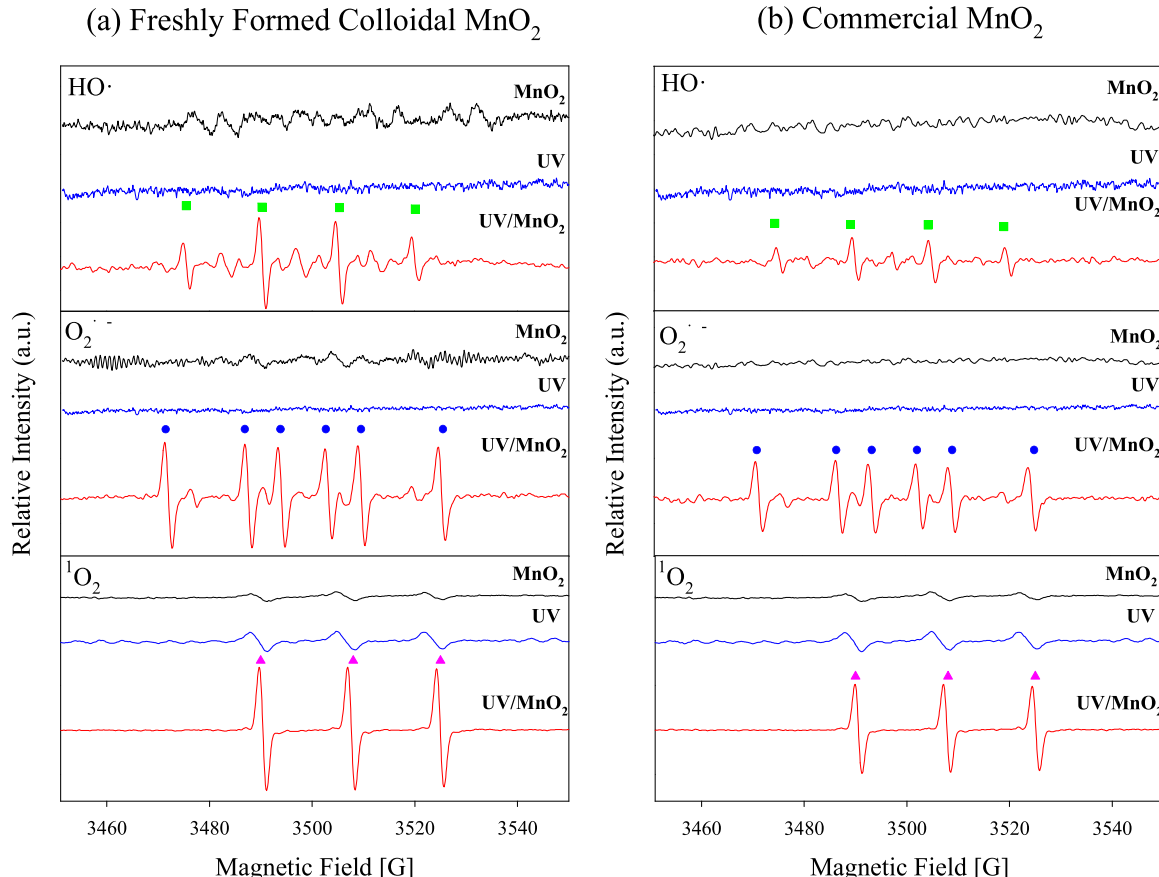


**Fig. 3.** Determination of reactive species formed in the UV/freshly formed colloidal  $\text{MnO}_2$  system (a) and the UV/commercial  $\text{MnO}_2$  system (b) at pH 7.0 by EPR spectra. Conditions:  $[\text{MnO}_2]_0 = 100 \mu\text{M}$ ,  $[\text{DMPO}]_0 = [\text{TEMP}]_0 = 0.45 \text{ M}$ . Reaction time = 10 min (■-  $\text{HO}^\bullet$ , ●-  $\text{O}_2^\bullet-$ , ▲-  $^1\text{O}_2$ ;  $\text{HO}^\bullet$  and  $^1\text{O}_2$  were detected in aqueous dispersion;  $\text{O}_2^\bullet-$  was detected in 50% methanol dispersion).

investigated. The potential VB value ( $E_{VB}$ ) of the freshly formed colloidal  $\text{MnO}_2$  was 1.18 eV from the VB-XPS spectra (Fig. S6a). The UV-vis absorption spectra of  $\text{MnO}_2$  are shown in Fig. S6b, from which  $E_g$  values of  $\text{MnO}_2$  were calculated to be 1.53 eV via Eq. 1,

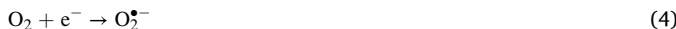
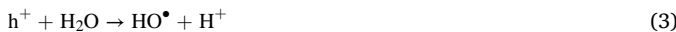
$$E_g = \frac{h \cdot c}{\lambda} \quad (1)$$

where  $h$  (Planck constant) is  $6.626 \times 10^{-34}$  J·s,  $c$  (speed of light) is  $3 \times 10^8$  m/s, and  $\lambda$  (nm) is the intersection abscissa of the baseline and the tangent at the spot where the slope is maximum on the UV-vis absorption spectrum [22].

Accordingly, the potential of the CB ( $E_{CB}$ ) value was calculated to be  $-0.35$  eV via Eq. 2.

$$E_g = E_{VB} - E_{CB} \quad (2)$$

Generally, the formation of  $\text{HO}^\bullet$  was ascribed to both the oxidative pathway (Eq. 3) and reductive pathways (Eq. 4–6) [22]. Eq. 3 could proceed when  $E_{VB}$  is higher than  $E_0(\text{HO}^\bullet/\text{H}_2\text{O}) = 2.31$  V<sub>NHE</sub> at pH 7, and Eq. 4 could take place when  $E_{CB}$  is more negative than  $E_0(\text{O}_2^\bullet/\text{O}_2) = -0.33$  V<sub>NHE</sub> [47]. Therefore,  $\text{HO}^\bullet$  cannot be produced by  $\text{h}^+$  generated by  $\text{MnO}_2$ , but it can be formed via reductive pathways. Moreover, when argon was purged into the test solution (dissolved oxygen was less than 0.3 mg/L), NB, an  $\text{HO}^\bullet$  probe, was not degraded in the UV/ $\text{MnO}_2$  system (Fig. S7). This result indicates that  $\text{HO}^\bullet$  could be generated only via Eqs. 4–6 and that the presence of oxygen is essential in ROS formation.



### 3.4. Roles of reactive species in the degradation of GFRZ and NDA by the UV/ $\text{MnO}_2$ system

As discussed above, UV photocatalysis of  $\text{MnO}_2$  generates  $\text{h}^+$  and  $\text{e}^-$ , which promotes the formation of ROS, including  $\text{HO}^\bullet$ ,  $\text{O}_2^\bullet$ ,  $\text{H}_2\text{O}_2$  and  $\text{O}_2$ . To specifically identify the contribution of  $\text{HO}^\bullet$  in the system, NB was used as a probe to measure the steady-state concentration of  $\text{HO}^\bullet$  and its contribution to total  $k'$  (details shown in Text S2). TBA and oxalate were added to the test solution to investigate the contribution of  $\text{HO}^\bullet$  and  $\text{h}^+$  to total  $k'$ , respectively.

Fig. 4 shows the roles of specific reactive species for the degradation of NDA and GFRZ in the UV/ $\text{MnO}_2$  system at pH 7 by using probes and different scavengers.  $\text{HO}^\bullet$  was not a dominant reactive species for target pollutant degradation. The contributions of  $\text{HO}^\bullet$  to the total  $k'$  were 10% and 21% for NDA and GFRZ, respectively, which were consistent with the inhibition rate of  $k'$  when using TBA as an  $\text{HO}^\bullet$  scavenger.  $\text{h}^+$  was the primary reactive species for the degradation of NDA, while both ROS and  $\text{h}^+$  accounted for the degradation of GFRZ. The contribution of UV photolysis to the total  $k'$  was 16% for NDA and 44% for GFRZ. The inhibition rates of  $k'$  of NDA and GFRZ using oxalate as a  $\text{h}^+$  scavenger were 53.3% and 26.2%, respectively, indicating that  $\text{h}^+$  formed in UV/ $\text{MnO}_2$  would contribute to 53.3% and 26.2%, respectively, of the total  $k'$  of NDA and GFRZ. The contribution of  $\text{h}^+$  is positively correlated to the adsorption of target pollutants. As shown in Fig. S4, the adsorption rate of NDA was higher than that of GFRZ; thus,  $\text{h}^+$  contributed more to the former.

To investigate the contribution of  $\text{e}^-$ , argon was purged into the solution to create oxygen-free conditions in which case  $\text{e}^-$  could not be transferred to ROS. When purging argon,  $k'$  decreased by 20% and 26.2% for NDA and GFRZ, respectively, and the formation of  $\text{HO}^\bullet$  was inhibited as NB was not degraded (Fig. S7). According to the above

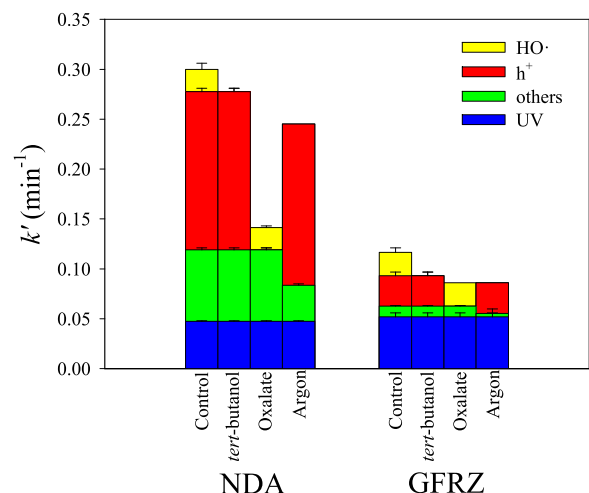


**Fig. 4.** The contributions of reactive species on the degradation of GFRZ and NDA in the UV/ $\text{MnO}_2$  system with or without quencher in pure water at pH 7. Conditions:  $[\text{MnO}_2]_0 = 100 \mu\text{M}$ ,  $[\text{NDA}]_0 = [\text{GFRZ}]_0 = 5 \mu\text{M}$ ,  $[\text{NB}]_0 = 1 \mu\text{M}$ ,  $[\text{TBA}]_0 = 2 \text{ mM}$ ,  $[\text{oxalate}]_0 = 1 \text{ mM}$ , argon was purged into the water for 30 min (dissolved oxygen  $< 0.3 \text{ mg/L}$ ).

discussion,  $\text{HO}^\bullet$  accounted for 10% and 21% of the  $k'$  of NDA and GFRZ, respectively. Therefore, other ROS (excluding  $\text{HO}^\bullet$ ) accounted for 10% and 5.2% of the  $k'$  of NDA and GFRZ, respectively. Then, the contribution of  $\text{e}^-$  to  $k'$  could be calculated to be 10.7% and 3.6% for NDA and GFRZ, respectively.

### 3.5. Degradation pathways of NDA and GFRZ in the UV/ $\text{MnO}_2$ system

Based on the products identified by UPLC-QTOF-MS, detailed information (i.e., elemental formula and structure) on the products formed during the degradation of NDA and GFRZ in the UV/ $\text{MnO}_2$  system is provided in Tables S4 and S5. The total ion chromatograms of NDA and GFRZ are shown in Figs. S8 and S11, respectively, and the MS and MS/MS spectra of the NDA and GFRZ main products are shown in Figs. S9 and S12, respectively.

Figs. S10 and S13 show the time-dependent evolution profiles of the main products of NDA and GFRZ, respectively. During the degradation of NDA by the UV/ $\text{MnO}_2$  system, 13 main products were detected, including  $m/z$  249a ( $\text{C}_{12}\text{H}_{13}\text{N}_2\text{O}_4$ ),  $m/z$  249b ( $\text{C}_{12}\text{H}_{13}\text{N}_2\text{O}_4$ ),  $m/z$  231 ( $\text{C}_{12}\text{H}_{11}\text{N}_2\text{O}_3$ ),  $m/z$  219 ( $\text{C}_{11}\text{H}_{11}\text{N}_2\text{O}_3$ ),  $m/z$  205 ( $\text{C}_{10}\text{H}_9\text{N}_2\text{O}_3$ ),  $m/z$  237 ( $\text{C}_{12}\text{H}_{11}\text{N}_2\text{O}_3$ ),  $m/z$  253 ( $\text{C}_{12}\text{H}_{11}\text{N}_2\text{O}_3$ ),  $m/z$  181 ( $\text{C}_9\text{H}_{13}\text{N}_2\text{O}_2$ ),  $m/z$  225 ( $\text{C}_{12}\text{H}_{11}\text{N}_2\text{O}_3$ ),  $m/z$  209 ( $\text{C}_9\text{H}_9\text{N}_2\text{O}_4$ ),  $m/z$  165 ( $\text{C}_9\text{H}_{13}\text{N}_2\text{O}_1$ ),  $m/z$  239 ( $\text{C}_{10}\text{H}_{11}\text{N}_2\text{O}_5$ ) and  $m/z$  247 ( $\text{C}_{12}\text{H}_{11}\text{N}_2\text{O}_3$ ). For GFRZ, four different isomers of  $m/z$  265 ( $\text{C}_{15}\text{H}_{22}\text{O}_4$ ), two different isomers of  $m/z$  263 ( $\text{C}_{15}\text{H}_{20}\text{O}_4$ ),  $m/z$  137 ( $\text{C}_8\text{H}_{10}\text{O}_2$ ),  $m/z$  145 ( $\text{C}_7\text{H}_{14}\text{O}_3$ ), and two isomers of  $m/z$  135 ( $\text{C}_8\text{H}_8\text{O}_2$ ) were detected.

Fig. 5a and b show the proposed degradation pathways of NDA and GFRZ in the UV/ $\text{MnO}_2$  system, respectively. During the degradation of NDA, the initial pathways included demethylation and side chain cleavage, forming  $m/z$  219,  $m/z$  231 and  $m/z$  205 via  $\text{h}^+$  attacks of the bond on the aromatic rings. Additionally,  $\text{HO}^\bullet$  attacks the electron-rich aromatic ring of NDA to produce  $m/z$  249a and  $m/z$  249b via hydroxylation, corresponding to previous studies [29,48–52]. Then, for the products at  $m/z$  219, hydroxylation via  $\text{HO}^\bullet$  at C7 and side chain cleavage via  $\text{h}^+$  and  $\text{HO}^\bullet$  at N1 occurred, resulting in the formation of  $m/z$  237 and  $m/z$  209. For  $m/z$  205, decarboxylation took place at C3 and formed one of the final products at  $m/z$  165. For  $m/z$  249a, side chain cleavage via  $\text{h}^+$  and decarboxylation via further oxidation by  $\text{h}^+$  and  $\text{HO}^\bullet$  could occur, resulting in the intermediate at  $m/z$  181. The  $m/z$  181 could be further converted into  $m/z$  165 via dehydroxylation. In addition, ring cleavage occurred at C2 = C3, while side chain cleavage and carboxylation occurred subsequently, resulting in the generation of

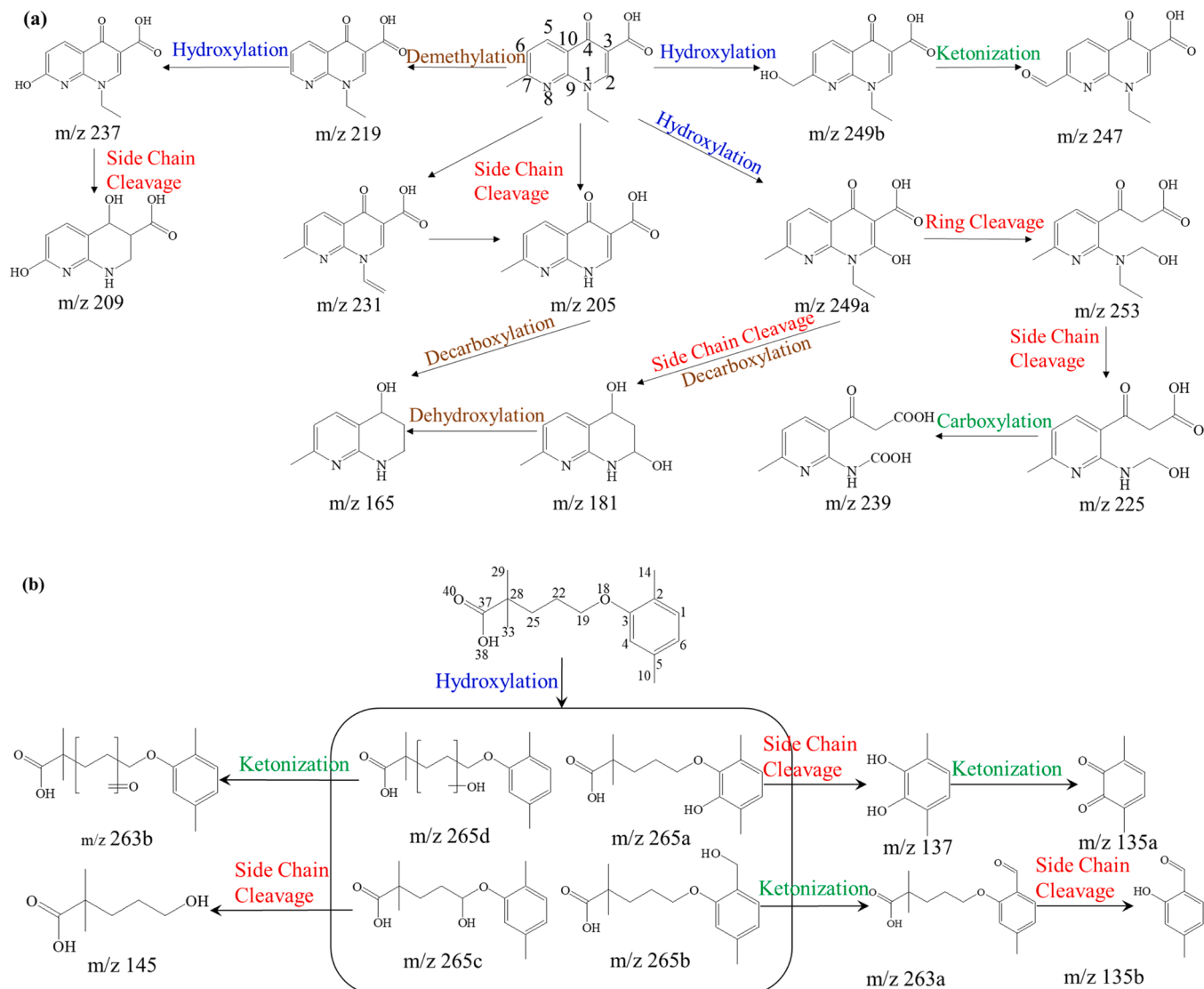


Fig. 5. Proposed degradation pathways of (a) NDA and (b) GFRZ by the UV/MnO<sub>2</sub> system.

*m/z* 253, *m/z* 225 and *m/z* 239. Finally, ketonization via HO<sup>•</sup> oxidation took place on the hydroxylated initial product at *m/z* 249b, resulting in the generation of the final products at *m/z* 247.

During the degradation of GFRZ, four hydroxylated products (*m/z* 265 isomers) were initially formed via HO<sup>•</sup> addition reactions at C4, C22 and C25 or H-abstraction reactions at C14 and C19 atoms [53]. Next, *m/z* 265a underwent side chain cleavage via h<sup>+</sup> to form diphenols at *m/z* 137 and ketonization via HO<sup>•</sup> oxidation to form quinones at *m/z* 135a in which h<sup>+</sup> is reported to attack the C-O bonds at C19 of GFRZ via side chain cleavage reactions [54]. Another hydroxylated product, *m/z* 265b, was further transformed to *m/z* 263a and *m/z* 135b via ketonization and side chain cleavage reactions. h<sup>+</sup> attacked *m/z* 265c, resulting in aliphatic acid (*m/z* 145) formation via the side chain cleavage reaction. Finally, *m/z* 265d generated via a HO<sup>•</sup> addition reaction on C22 and C25 of GFRZ went through the ketonization reaction to form *m/z* 263b.

In summary, side chain cleavage, ketonization and hydroxylation were found during the degradation of both NDA and GFRZ by the UV/freshly formed MnO<sub>2</sub> system, while extra degradation pathways, including ring cleavage, demethylation and decarboxylation, could also take place during NDA degradation.

### 3.6. Effects of MnO<sub>2</sub> dosage and pH

Fig. 6a and b show the *k*'s of NDA and GFRZ by UV/MnO<sub>2</sub> at MnO<sub>2</sub> dosages of 50, 100, and 200  $\mu$ M. As the MnO<sub>2</sub> dosage rose from 50  $\mu$ M to 100  $\mu$ M, the *k*' of NDA increased by 116.7% (from  $0.138 \text{ min}^{-1}$  to  $0.299 \text{ min}^{-1}$ ), while it slightly increased by 9.0% when the MnO<sub>2</sub> dosage was further increased from 100  $\mu$ M to 200  $\mu$ M (Fig. 6a). In comparison, increasing MnO<sub>2</sub> levels from 50  $\mu$ M to 100  $\mu$ M increased the *k*' of GFRZ by 38.1% (from  $0.084 \text{ min}^{-1}$  to  $0.116 \text{ min}^{-1}$ ) but slightly decreased it by 19.0% with increasing MnO<sub>2</sub> from 100  $\mu$ M to 200  $\mu$ M ( $0.094 \text{ min}^{-1}$ ) (Fig. 6b). The increasing *k*'s of NDA and GFRZ were nonlinear as a function of MnO<sub>2</sub> dosage. This could be attributed to the shadow effect of MnO<sub>2</sub>, which inhibited UV utilization and the formation of reactive species (h<sup>+</sup> and e<sup>-</sup>).

The effect of pH on the degradation of NDA and GFRZ in the UV/MnO<sub>2</sub> system is shown in Figs. 6c and 6d. As the pH decreased from 8 to 6, the *k*' of NDA increased from  $0.057 \text{ min}^{-1}$  to  $0.367 \text{ min}^{-1}$ , while the *k*' of GFRZ peaked at pH 7 ( $0.116 \text{ min}^{-1}$ ) and that was similar at pH 6 and 8. The lower pH facilitated the migration of e<sup>-</sup> from the surface of MnO<sub>2</sub> and decreased the recombination of h<sup>+</sup> [55]; thus, more h<sup>+</sup> was utilized to attack target pollutants, which accounted for the increasing *k*' of NDA. Interestingly, the *k*' of GFRZ had a different trend compared to NDA, which might be attributed to the better adsorption rate of GFRZ by MnO<sub>2</sub>.

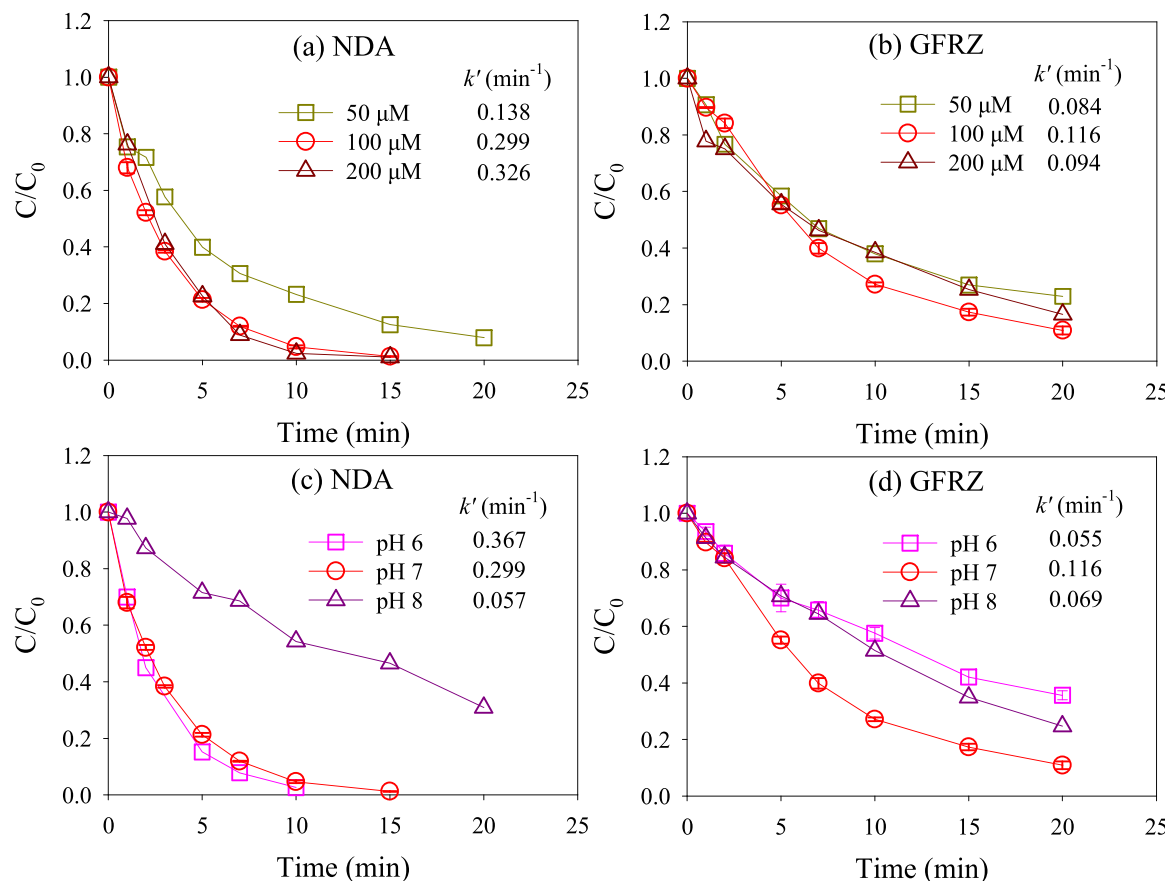


**Fig. 6.** Effects of  $\text{MnO}_2$  dosage (a – b) and pH (c – d) on the NDA and GFRZ degradation in the UV/ $\text{MnO}_2$  system. Conditions:  $[\text{MnO}_2] = 50, 100, 200 \mu\text{M}$ ,  $[\text{NDA}]_0 = [\text{GFRZ}]_0 = 5 \mu\text{M}$ , pH = 7 for a and b;  $[\text{NDA}]_0 = [\text{GFRZ}]_0 = 5 \mu\text{M}$ ,  $[\text{MnO}_2] = 100 \mu\text{M}$  for c and d.

at pH 7. The mechanism of pH influence on UV/freshly formed colloidal  $\text{MnO}_2$  requires further research.

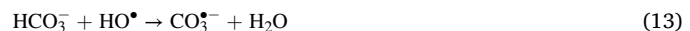
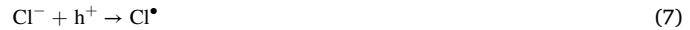
### 3.7. Effects of water matrices

Water matrix components such as  $\text{Cl}^-$ ,  $\text{SO}_4^{2-}$ ,  $\text{HCO}_3^-$  and NOM are ubiquitous in drinking water at the concentrations of 0.024 – 1.5 mM, 0.16 – 4.1 mM, 0.01 – 2.4 mM, 1 – 10 mg C/L, respectively [56,57]. Herein, 1 mM  $\text{Cl}^-$ , 1 mM  $\text{SO}_4^{2-}$ , 1 mM  $\text{HCO}_3^-$  and 2 mg C/L NOM were individually spiked into the solution to investigate their effects on the UV/freshly formed colloidal  $\text{MnO}_2$  system. Fig. 7 shows the effects of water matrices on the degradation of NDA and GFRZ by the UV/ $\text{MnO}_2$  system at pH 7 in pure water. Overall, 1 mM  $\text{SO}_4^{2-}$  had negligible effects on the degradation of both NDA and GFRZ. In contrast,  $\text{Cl}^-$  at 1 mM,  $\text{HCO}_3^-$  at 1 mM, and NOM at 2 mg C/L decreased the degradation of NDA and GFRZ. For NDA,  $k'$  was slightly decreased by 6% at 1 mM  $\text{Cl}^-$ , while it was remarkably decreased by 59% and 36% with  $\text{HCO}_3^-$  (1 mM) and NOM (2 mg C/L), respectively. Compared to the control tests, the  $k'$  of GFRZ was significantly decreased by 26%, 43% and 37% in the presence of  $\text{Cl}^-$ ,  $\text{HCO}_3^-$  and NOM, respectively.

$\text{Cl}^-$  and  $\text{HCO}_3^-$  are known to scavenge  $\text{h}^+$  and  $\text{HO}^\bullet$  to form reactive chlorine species (RCS, i.e.,  $\text{Cl}^\bullet$  and  $\text{Cl}_2^\bullet$ ) (Eq. 7–11) and  $\text{CO}_3^{2-}$  (Eqs. 12 and 13), respectively [58–60]. Although the redox potentials of  $\text{Cl}^\bullet$  (2.4 V) and  $\text{Cl}_2^\bullet$  (2.0 V) are considerable, they are more selective oxidants to attack micropollutants containing electron-donating groups compared to  $\text{h}^+$  and nonselective  $\text{HO}^\bullet$  [31].  $\text{CO}_3^{2-}$  has a relatively lower reactivity towards micropollutants [59].

Herein,  $\text{h}^+$  is the dominant reactive species for both NDA and GFRZ abatement in the UV/ $\text{MnO}_2$  system. Thus,  $\text{Cl}^-$  and  $\text{HCO}_3^-$  consumed  $\text{h}^+$ , and the contribution of the formed radical species could not offset the

loss of  $\text{h}^+$ , resulting in a decrease in the  $k'$ s of NDA and GFRZ.



NOM is a common  $\text{HO}^\bullet$  scavenger, and the second-order rate constant of NOM with  $\text{HO}^\bullet$  is  $1.4 \times 10^4 \text{ L}^{-1} (\text{mg C})^{-1} \text{ s}^{-1}$ . NOM (2 mg C/L) was calculated to quench 46.6% and 39.8%  $\text{HO}^\bullet$  during the degradation of NDA and GFRZ, respectively [59]; thus, the  $k'$ s of NDA and GFRZ were calculated to decrease by 4.7% and 8.4%, respectively, via  $\text{HO}^\bullet$  scavenging. Also, NOM in water filtered UV light [61]; thus, it significantly decreased the  $k'$ s of NDA and GFRZ by 36.7% and 48.1%, respectively, by UV direct photolysis (Fig. S14). Also, the filter of UV light can suppress the photocatalytic efficiency of  $\text{MnO}_2$ , resulting in the decreased formation of reactive species. More importantly, NOM contains carboxylic groups and can be adsorbed on photocatalysts and then can scavenge  $\text{h}^+$ . Therefore, the remarkable inhibition of  $k'$ s by NOM was ascribed to the consumption of  $\text{h}^+$  [62].

## 4. Conclusions

Freshly formed colloidal  $\text{MnO}_2$  acted as a photocatalyst. ROS,

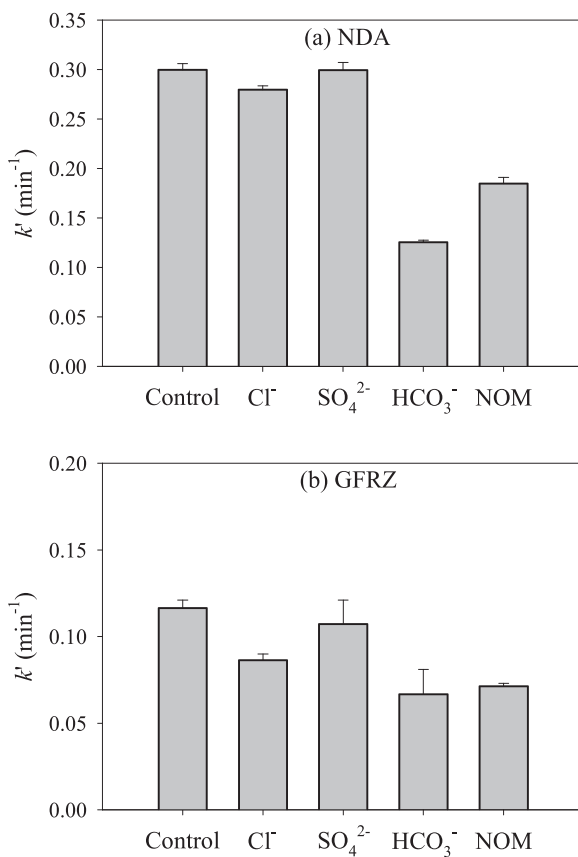


**Fig. 7.** Effects of water matrices on the degradation of (a) NDA and (b) GFRZ in the UV/freshly formed  $\text{MnO}_2$  system at pH 7 in pure water. Conditions:  $[\text{MnO}_2]_0 = 100 \mu\text{M}$ ,  $[\text{GFRZ}]_0 = [\text{NDA}]_0 = 5 \mu\text{M}$ ,  $[\text{Cl}^-]_0 = [\text{SO}_4^{2-}]_0 = [\text{HCO}_3^-]_0 = 1 \text{ mM}$ ,  $[\text{NOM}]_0 = 2 \text{ mg C/L}$ .

including  $\text{HO}^\bullet$ ,  $\text{O}_2^\bullet$ , and  ${}^1\text{O}_2$ , could form solely via reductive pathways, while  $\text{h}^+$  could be directly degraded in the UV/ $\text{MnO}_2$  system. NDA and GFRZ showed obviously increasing degradation by the UV/freshly formed colloidal  $\text{MnO}_2$  system.  $\text{h}^+$  showed a predominant contribution to NDA degradation, while the roles of  $\text{h}^+$  and ROS in GFRZ degradation were approximately equal. With increasing  $\text{MnO}_2$  dose,  $k'$  for GFRZ and NDA increased nonlinearly owing to the shadow effect of  $\text{MnO}_2$ .  $\text{Cl}^-$ ,  $\text{HCO}_3^-$ , and NOM inhibited  $k'$  for NDA and GFRZ due to the major consumption of  $\text{h}^+$  and minor consumption of ROS. Side chain cleavage via  $\text{h}^+$ , kentonization and hydroxylation via  $\text{HO}^\bullet$  were the major degradation pathways during NDA and GFRZ degradation by UV/freshly formed colloidal  $\text{MnO}_2$ . Ring cleavage, demethylation and decarboxylation could also occur during NDA degradation.

The present work suggests that the photocatalytic effect of freshly formed colloidal  $\text{MnO}_2$  could be a useful approach for the degradation of micropollutants. The system is applicable because  $\text{MnO}_2$  as a residual after permanganate preoxidation in water treatment could be utilized to remove organic micropollutants.

#### CRediT authorship contribution statement

**Wenrui Wei:** Investigation, Data curation, Writing – original draft, Writing – review & editing, Experiment. **Anna Wang:** Investigation, Data curation, Writing – review & editing, Experiment. **Ailin Li:** Investigation, Data curation, Experiment. **Xinwen Kang:** Investigation, Data curation. **Kaiheng Guo:** Data curation, Writing – review & editing. **Shaoxiong He:** Data curation, Writing – review & editing. **Jingyun Fang:** Writing – review & editing, Supervision.

#### Declaration of Competing Interest

The authors declare that they have no known competing financial interests or personal relationships that could have appeared to influence the work reported in this paper.

#### Acknowledgements

This work was financially supported by the Natural Science Foundation of China (grants 21922612), the Fundamental Research Funds for the Central Universities (20lgjc02), the China Postdoctoral Science Foundation (2021M703676) and the Guangdong Basic and Applied Basic Research Foundation (2021A1515110973).

#### Appendix A. Supporting information

Supplementary data associated with this article can be found in the online version at [doi:10.1016/j.apcatb.2022.121441](https://doi.org/10.1016/j.apcatb.2022.121441).

#### References

- [1] J.E. Post, Manganese oxide minerals: Crystal structures and economic and environmental significance, *Proc. Natl. Acad. Sci. USA* 96 (1999) 3447–3454.
- [2] I. Kruck, P. Zajdel, W. van Beek, I. Bakaimi, A. Lappas, C. Stock, M.A. Green, Coupled commensurate cation and charge modulation in the tunneled structure,  $\text{Na}_{0.40(2)}\text{MnO}_2$ , *J. Am. Chem. Soc.* 133 (2011) 13950–13956.
- [3] S. Chen, J. Zhu, X. Wu, Q. Han, X. Wang, Graphene oxide– $\text{MnO}_2$  nanocomposites for supercapacitors, *ACS Nano* 4 (2010) 2822–2830.
- [4] C.K. Remucal, M. Ginder-Vogel, A critical review of the reactivity of manganese oxides with organic contaminants, *Environ. Sci. Proc. Imp.* 16 (2014) 1247–1266.
- [5] D. Wang, J.Y. Shin, M.A. Cheney, G. Sposito, T.G. Spiro, Manganese dioxide as a catalyst for oxygen-independent atrazine dealkylation, *Environ. Sci. Technol.* 33 (1999) 3160–3165.
- [6] J. Jiang, Y. Gao, S. Pang, X. Lu, Y. Zhou, J. Ma, Q. Wang, Understanding the role of manganese dioxide in the oxidation of phenolic compounds by aqueous permanganate, *Environ. Sci. Technol.* 49 (2015) 520–528.
- [7] R. Yang, Y. Fan, R. Ye, Y. Tang, X. Cao, Z. Yin, Z. Zeng,  $\text{MnO}_2$ -based materials for environmental applications, *Adv. Mater.* 33 (2021), 2004862.
- [8] K. Guo, J. Zhang, A. Li, R. Xie, Z. Liang, A. Wang, L. Ling, X. Li, C. Li, J. Fang, Ultraviolet irradiation of permanganate enhanced the oxidation of micropollutants by producing  $\text{HO}^\bullet$  and reactive manganese species, *Environ. Sci. Tech. Let.* 5 (2018) 750–756.
- [9] Y. Liu, Y. Li, L. Wang, W. Wang, J. Ma, Enhanced trace Tl removal with ferrate through the addition of Mn(II): Effect and mechanism, *ACS EST Eng.* 1 (2021) 571–580.
- [10] X. Cai, Q. Liu, C. Xia, D. Shan, J. Du, J. Chen, Recyclable capture and destruction of aqueous micropollutants using the molecule-specific cavity of cyclodextrin polymer coupled with  $\text{KMnO}_4$  oxidation, *Environ. Sci. Technol.* 49 (2015) 9264–9272.
- [11] Y. Guo, S. Zhu, B. Wang, J. Huang, S. Deng, G. Yu, Y. Wang, Modelling of emerging contaminant removal during heterogeneous catalytic ozonation using chemical kinetic approaches, *J. Hazard. Mater.* 380 (2019), 120888.
- [12] J.G. Mahy, C. Wolfs, C. Vreuls, S. Drot, S. Dircks, A. Boergers, J. Tuerk, S. Hermans, S.D. Lambert, Advanced oxidation processes for waste water treatment: from laboratory-scale model water to on-site real waste water, *Environ. Technol.* 42 (2021) 3974–3986.
- [13] S.M.Z. Andrabí, Z. Khan, Reactivity of some sulphur- and non-sulphur-containing amino acids towards water soluble colloidal  $\text{MnO}_2$ . A kinetic study, *Colloid Polym. Sci.* 285 (2006) 389–396.
- [14] M.A. Islam, M.M. Rahman, Soluble colloidal manganese dioxide: Formation, identification and prospects of application, *Colloid.* J 75 (2013) 538–542.
- [15] Y. Liu, X. Zhang, J. Bian, J. Sun, Z. Li, I. Khan, Y. Qu, Z. Li, Z. Jiang, L. Jing, Promoted oxygen activation of layered micro-mesoporous structured titanium phosphate nanoplates by coupling nano-sized  $\delta\text{-MnO}_2$  with surface pits for efficient photocatalytic oxidation of CO, *Appl. Catal. B: Environ.* 254 (2019) 260–269.
- [16] L. Chen, J. Jia, R. Ran, X. Song, Nickel doping  $\text{MnO}_2$  with abundant surface pits as highly efficient catalysts for propane deep oxidation, *Chem. Eng. J.* 369 (2019) 1129–1137.
- [17] D. Xia, H. Liu, B. Xu, Y. Wang, Y. Liao, Y. Huang, L. Ye, C. He, P.K. Wong, R. Qiu, Single Ag atom engineered 3D- $\text{MnO}_2$  porous hollow microspheres for rapid photothermocatalytic inactivation of *E. coli* under solar light, *Appl. Catal. B: Environ.* 245 (2019) 177–189.
- [18] M. Dubey, N.V. Challagulla, S. Wadhwa, R. Kumar, Ultrasound assisted synthesis of magnetic  $\text{Fe}_3\text{O}_4/\alpha\text{-MnO}_2$  nanocomposite for photodegradation of organic dye, *Colloid Surf. A* 609 (2021), 125720.
- [19] M. Ma, Y. Yang, Y. Chen, Y. Ma, P. Lyu, A. Cui, W. Huang, Z. Zhang, Y. Li, F. Si, Photocatalytic degradation of MB dye by the magnetically separable 3D flower-like  $\text{Fe}_3\text{O}_4/\text{SiO}_2/\text{MnO}_2/\text{BiOBr-Bi}$  photocatalyst, *J. Alloy. Compd.* 861 (2021), 158256.
- [20] S. Sekar, S. Lee, P. Vijayarengan, K.M. Kalirajan, T. Santhakumar, S. Sekar, S. Sadhasivam, Upcycling of wastewater via effective photocatalytic hydrogen

production using  $\text{MnO}_2$  nanoparticles—Decorated activated carbon nanoflakes, *Nanomat.* **Basel** **10** (2020) 1610.

[21] J. Zhao, Z. Zhao, N. Li, J. Nan, R. Yu, J. Du, Visible-light-driven photocatalytic degradation of ciprofloxacin by a ternary  $\text{Mn}_2\text{O}_3/\text{Mn}_3\text{O}_4/\text{MnO}_2$  valence state heterojunction, *Chem. Eng. J.* **353** (2018) 805–813.

[22] W. Dou, X. Hu, L. Kong, X. Peng, UV-improved removal of chloride ions from strongly acidic wastewater using  $\text{Bi}_2\text{O}_3$ : Efficiency enhancement and mechanisms, *Environ. Sci. Technol.* **53** (2019) 10371–10378.

[23] J. Zhao, J. Nan, Z. Zhao, N. Li, J. Liu, F. Cui, Energy-efficient fabrication of a novel multivalence  $\text{Mn}_3\text{O}_4\text{-MnO}_2$  heterojunction for dye degradation under visible light irradiation, *Appl. Catal. B: Environ.* **202** (2017) 509–517.

[24] S. Das, A. Samanta, S. Jana, Light-assisted synthesis of hierarchical flower-like  $\text{MnO}_2$  nanocomposites with solar light induced enhanced photocatalytic activity, *ACS Sustain. Chem. Eng.* **5** (2017) 9086–9094.

[25] A. Baral, D.P. Das, M. Minakshi, M.K. Ghosh, D.K. Padhi, Probing environmental remediation of RhB organic dye using  $\alpha\text{-MnO}_2$  under visible-light irradiation: structural, photocatalytic and mineralization studies, *Chemistryselect* **1** (2016) 4277–4285.

[26] A. Mehta, A. Mishra, S. Basu, Fluorescent carbon dot decorated  $\text{MnO}_2$  nanorods for complete photomineralization of phenol from water, *Environ. Sci. Water Res.* **4** (2018) 2012–2020.

[27] R. Yin, C. Shang, Removal of micropollutants in drinking water using UV-LED/chlorine advanced oxidation process followed by activated carbon adsorption, *Water Res.* **185** (2020), 116297.

[28] B. Díaz-Garduño, M.G. Pintado-Herrera, M. Biel-Maeso, J.J. Rueda-Márquez, P. A. Lara-Martín, J.A. Perales, M.A. Manzano, C. Garrido-Pérez, M.L. Martín-Díaz, Environmental risk assessment of effluents as a whole emerging contaminant: Efficiency of alternative tertiary treatments for wastewater depuration, *Water Res.* **119** (2017) 136–149.

[29] C. Sirtori, A. Zapata, W. Gernjak, S. Malato, A. Lopez, A. Agüera, Solar photo-Fenton degradation of nalidixic acid in waters and wastewaters of different composition. Analytical assessment by LC-TOF-MS, *Water Res.* **45** (2011) 1736–1744.

[30] H. Kjeldal, N.A. Zhou, D.K. Wissenbach, M. von Bergen, H.L. Gough, J.L. Nielsen, Genomic, proteomic, and metabolite characterization of gemfibrozil-degrading organism *Bacillus sp.* GeD10, *Environ. Sci. Technol.* **50** (2016) 744–755.

[31] J. Fang, Y. Fu, C. Shang, The roles of reactive species in micropollutant degradation in the UV/free chlorine system, *Environ. Sci. Technol.* **48** (2014) 1859–1868.

[32] Y. Song, J. Jiang, W. Qin, J. Zhu, J. Gu, J. Ma, Simultaneous photometric determination of oxidation kinetics and average manganese valence in manganese products in situ formed in the reactions of aqueous permanganate with model organic compounds and natural organic matters, *Sep. Purif. Technol.* **256** (2021), 117774.

[33] J.R. Bolton, K.G. Linden, Standardization of methods for fluence (UV Dose) determination in bench-scale UV experiments, *J. Environ. Eng.* **129** (2003) 209–215.

[34] X. Zhang, K. Guo, Y. Wang, Q. Qin, Z. Yuan, J. He, C. Chen, Z. Wu, J. Fang, Roles of bromine radicals,  $\text{HOBr}$  and  $\text{Br}_2$  in the transformation of flumequine by the UV/chlorine process in the presence of bromide, *Chem. Eng. J.* **400** (2020), 125222.

[35] E. Saputra, S. Muhammad, H. Sun, H.M. Ang, M.O. Tadé, S. Wang, Different crystallographic one-dimensional  $\text{MnO}_2$  nanomaterials and their superior performance in catalytic phenol degradation, *Environ. Sci. Technol.* **47** (2013) 5882–5887.

[36] S. Laha, R.G. Luthy, Oxidation of aniline and other primary aromatic amines by manganese dioxide, *Environ. Sci. Technol.* **24** (1990) 363–373.

[37] M. Wang, G. Zhang, G. Qiu, D. Cai, Z. Wu, Degradation of herbicide (glyphosate) using sunlight-sensitive  $\text{MnO}_2/\text{C}$  catalyst immediately fabricated by high energy electron beam, *Chem. Eng. J.* **306** (2016) 693–703.

[38] K. Saravananakumar, V. Muthuraj, S. Vadivel, Constructing novel Ag nanoparticles anchored on  $\text{MnO}_2$  nanowires as an efficient visible light driven photocatalyst, *RSC Adv.* **6** (2016) 61357–61366.

[39] G. Dong, B. Chen, B. Liu, S.R. Stoyanov, Y. Cao, M. Yang, B. Zhang, UV stimulated manganese dioxide for the persulfate catalytic degradation of bisphenol A, *Catalysts* **11** (2021) 502.

[40] A. Eslami, M. Hashemi, F. Ghanbari, Degradation of 4-chlorophenol using catalyzed peroxymonosulfate with nano- $\text{MnO}_2$ /UV irradiation: Toxicity assessment and evaluation for industrial wastewater treatment, *J. Clean. Prod.* **195** (2018) 1389–1397.

[41] Q. Li, L. Wang, X. Fang, L. Zhang, J. Li, H. Xie, Synergistic effect of photocatalytic degradation of hexabromocyclododecane in water by UV/ $\text{TiO}_2$ /persulfate, *Catalysts* **9** (2019) 189.

[42] C. Song, L. Wang, J. Ren, B. Lv, Z. Sun, J. Yan, X. Li, J. Liu, Comparative study of diethyl phthalate degradation by UV/ $\text{H}_2\text{O}_2$  and UV/ $\text{TiO}_2$ : Kinetics, mechanism, and effects of operational parameters, *Environ. Sci. Pollut. R.* **23** (2016) 2640–2650.

[43] L. Ren, D. Zhou, J. Wang, T. Zhang, Y. Peng, G. Chen, Biomaterial-based flower-like  $\text{MnO}_2$ @ carbon microspheres for rapid adsorption of amoxicillin from wastewater, *J. Mol. Liq.* **309** (2020), 113074.

[44] F. Rahnama, H. Ashrafi, M. Akhond, G. Absalan, Introducing  $\text{Ag}_2\text{O}\text{-Ag}_2\text{CO}_3\text{/rGO}$  nanoadsorbents for enhancing photocatalytic degradation rate and efficiency of Congo red through surface adsorption, *Colloid Surf. A* **613** (2021), 126068.

[45] J. Clément, N. Ferré, D. Siri, H. Karoui, A. Rockenbauer, P. Tordo, Assignment of the EPR spectrum of 5,5-Dimethyl-1-pyrroline N-oxide (DMPO) superoxide spin adduct, *J. Org. Chem.* **70** (2005) 1198–1203.

[46] C. Dong, Y. Bao, T. Sheng, Q. Yi, Q. Zhu, B. Shen, M. Xing, I.M.C. Lo, J. Zhang, Singlet oxygen triggered by robust bimetallic  $\text{MoFe}/\text{TiO}_2$  nanospheres of highly efficacy in solar-light-driven peroxymonosulfate activation for organic pollutants removal, *Appl. Catal. B: Environ.* **286** (2021), 119930.

[47] J. Lim, H. Kim, J. Park, G. Moon, J.J.M. Vequizo, A. Yamakata, J. Lee, W. Choi, How  $\text{g-C}_3\text{N}_4$  works and is different from  $\text{TiO}_2$  as an environmental photocatalyst: Mechanistic view, *Environ. Sci. Technol.* **54** (2020) 497–506.

[48] Y. Guo, W. Shi, Y. Zhu, Y. Xu, F. Cui, Enhanced photoactivity and oxidizing ability simultaneously via internal electric field and valence band position by crystal structure of bismuth oxyiodide, *Appl. Catal. B: Environ.* **262** (2020), 118262.

[49] Z. Wu, J. Shen, N. Ma, Z. Li, M. Wu, D. Xu, S. Zhang, W. Feng, Y. Zhu,  $\text{Bi}_4\text{O}_5\text{Br}_2$  nanosheets with vertical aligned facets for efficient visible-light-driven photodegradation of BPA, *Appl. Catal. B: Environ.* **286** (2021), 119937.

[50] A. Khataee, T.S. Rad, M. Fathinia, The role of clinoptilolite nanosheets in catalytic ozonation process: Insights into the degradation mechanism, kinetics and the toxicity, *J. Taiwan Inst. Chem. E.* **77** (2017) 205–215.

[51] Z. Li, P. Zhang, T. Shao, X. Li,  $\text{In}_2\text{O}_3$  nanoporous nanosphere: A highly efficient photocatalyst for decomposition of perfluoroctanoic acid, *Appl. Catal. B: Environ.* **125** (2012) 350–357.

[52] X. Li, P. Zhang, L. Jin, T. Shao, Z. Li, J. Cao, Efficient photocatalytic decomposition of perfluoroctanoic acid by indium oxide and its mechanism, *Environ. Sci. Technol.* **46** (2012) 5528–5534.

[53] P. Chen, F. Wang, Z. Chen, Q. Zhang, Y. Su, L. Shen, K. Yao, Y. Liu, Z. Cai, W. Lv, G. Liu, Study on the photocatalytic mechanism and detoxicity of gemfibrozil by a sunlight-driven  $\text{TiO}_2$ /carbon dots photocatalyst: The significant roles of reactive oxygen species, *Appl. Catal. B: Environ.* **204** (2017) 250–259.

[54] S. Yurdakal, V. Loddio, V. Augugliaro, H. Berber, G. Palmisano, L. Palmisano, Photodegradation of pharmaceutical drugs in aqueous  $\text{TiO}_2$  suspensions: Mechanism and kinetics, *Catal. Today* **129** (2007) 9–15.

[55] H. Kim, K. Kim, S. Park, W. Kim, S. Kim, J. Kim, Titanium dioxide surface modified with both palladium and fluoride as an efficient photocatalyst for the degradation of urea, *Sep. Purif. Technol.* **209** (2019) 580–587.

[56] A. Wang, Z. Hua, C. Chen, W. Wei, B. Huang, S. Hou, X. Li, J. Fang, Radical chemistry and PPCP degradation in the UV/peroxydisulfate process in the presence of chloride at freshwater levels, *Chem. Eng. J.* **426** (2021), 131276.

[57] I. Levchuk, J.J. Rueda Márquez, M. Sillanpää, Removal of natural organic matter (NOM) from water by ion exchange – A review, *Chemosphere* **192** (2018) 90–104.

[58] F. Li, L. Sun, Y. Liu, X. Fang, C. Shen, M. Huang, Z. Wang, D.D. Dionysiou, A  $\text{ClO}\bullet$ -mediated photoelectrochemical filtration system for highly-efficient and complete ammonia conversion, *J. Hazard. Mater.* **400** (2020), 123246.

[59] H. Ding, J. Hu, Enhancing the degradation of carbamazepine by UVA-LED/ $\text{WO}_3$  process with peroxydisulfate: Effects of light wavelength and water matrix, *J. Hazard. Mater.* **404** (2021), 124126.

[60] J.E. Grebel, J.J. Pignatello, W.A. Mitch, Effect of halide ions and carbonates on organic contaminant degradation by hydroxyl radical-based advanced oxidation processes in saline waters, *Environ. Sci. Technol.* **44** (2010) 6822–6828.

[61] Z. Wu, C. Chen, B. Zhu, C. Huang, T. An, F. Meng, J. Fang, Reactive nitrogen species are also involved in the transformation of micropollutants by the UV/monomochloramine process, *Environ. Sci. Technol.* **53** (2019) 11142–11152.

[62] M. Ren, M. Drosos, F.H. Frimmel, Inhibitory effect of NOM in photocatalysis process: Explanation and resolution, *Chem. Eng. J.* **334** (2018) 968–975.